IEEE Access
Multidisciplinary ⋮ Rapid Review ⋮ Open Access Journal

Received 4 October 2024, accepted 8 November 2024, date of publication 18 November 2024, date of current version 26 November 2024.

Digital Object Identifier 10.1109/ACCESS.2024.3500008

RESEARCH ARTICLE

Analytical Equivalent Circuit Extraction of Foreign Metal Objects in WPT Systems

RYO SHIRAI [1], (Member, IEEE), GORO NAKAO [2], AND MASANORI HASHIMOTO [1], (Senior Member, IEEE)
[1]Department of Informatics, Kyoto University, Kyoto 606-8501, Japan
[2]Device and Module Solutions Company, OMRON Corporation, Okayama 700-0927, Japan

Corresponding author: Ryo Shirai (shirai@i.kyoto-u.ac.jp)

This work was supported by JSPS KAKENHI Grant Number JP22K17867.

ABSTRACT Wireless power transfer (WPT) technologies are rapidly attracting attention because of their wide application field. Among them, inductive power transfer (IPT) technology is most promising for daily usage in households. Foreign metal detection (FMD) is indispensable for IPT applications because foreign metal heats up easily in the magnetic field generated by IPT devices and causes a dangerous situation. On the other hand, the representation of the foreign metal as an equivalent circuit model is not readily available. Therefore, we need to use finite element method (FEM)-based electromagnetic field simulators, which require massive computation time and cost. This work proposes a novel simulation method of foreign metal in the magnetic field based on theoretical analysis. We establish an equation-based theory for simulating metal pieces as circuit elements and deliver an equivalent circuit model with a virtual inductance of the metal piece and a mutual inductance between the sense coil and the metal piece. The Z parameter of the extracted circuit model is compared with that of a FEM-based simulator. Evaluation results show that the proposed method returns the result 971 times faster than the FEM-based simulator with the memory usage of 1/3863, while the simulation error is at most 3.88 %.

INDEX TERMS Foreign metal detection (FMD), electromagnetic field analysis, circuit analysis, numerical integration, wireless power transfer (WPT).

I. INTRODUCTION

For over a century, research on wireless power transfer (WPT) systems has been actively conducted, beginning with N. Tesla's first WPT experiment [1]. In recent decades, efforts to enhance efficiency [2], improve robustness [3], and expand application [4] have advanced significantly, leading to many important findings [5], [6], [7]. Besides, WPT technologies are widely used in various applications, such as smartphone chargers, personal computers, and tablets [5], [8].

WPT technologies are classified into five types according to the energy transmission medium [7]:

- acoustic power transfer (APT) [9], [10], [11], [12], [13], [14], [15],
- optical power transfer (OPT) [16], [17], [18],
- microwave power transfer (MPT) [19], [20], [21],
- capacitive power transfer (CPT) [7], [22],
- inductive power transfer (IPT) [2], [23].

Let us review each technology briefly. APT and OPT systems can achieve high power transmission efficiency; however, they suffer from a signal directivity problem, making them less versatile for WPT applications [11], [13], [16]. MPT systems also suffer from signal directivity problems and are therefore limited to two specific applications: application requiring long-distance energy transfer with high directivity [19] and application requiring only small amount of energy [21].

CPT systems are applicable to only the WPT system that requires short-distance power transfer, such as several millimeter to centimeter, while the IPT systems can apply to both millimeter-scale and meter-scale WPT [22], [24]. CPT systems can handle large power in the kilowatt range [22] while IPT handles less power than CPT due to eddy-current

The associate editor coordinating the review of this manuscript and approving it for publication was Salvatore Surdo.

and conductor losses [7]. Nevertheless, IPT system remains prevalent in applications requiring short-distance power transfer thanks to its versatility and widespread adoption [7].

Ref. [4] discusses safety issue of IPT system in terms of both living object detection (LOD) and foreign metal detection (FMD). Regarding LOD, high frequency signal can cause damage to human body, shown in safety standard (IEEE C95.1-2019) [25]. When the system is implemented in small volume, the coil size also becomes small, and consequently the resonance frequency increases [26], [27], [28]. However, the dangerous situation is avoidable as long as the designed system complies with the safety standard. Therefore, LOD is not considered a critical issue preventing WPT systems from entering the market. Meanwhile, IPT systems have to monitor foreign metals with special attention since those can cause system damage and failure [29]. Qi standard [30] is a well-known WPT standard, and Qi version 1.1 allows the system to transfer up to 5W power to devices. Here, suppose 0.5 W is dissipated in a small metallic object such as a coin and gold ring. In this case, the object temperature easily increases to more than 80°C [5]. To address such safety concerns, many FMD methods have been proposed, as will be detailed in Section II.

As promising FMD methods, electromagnetic field based methods are attracting attention since the sensing components of those methods are compatible with the power transmitting components of IPT systems. Here, for designing the FMD function and ensuring the system safety, designers need to estimate the impact of the foreign metal on the system. One tractable approach is to have an appropriate circuit model that reproduces the impact of the foreign metal. Especially, an accurate circuit model that captures the impact of small metal pieces is essential, as these small objects pose significant safety risks but are difficult to detect compared to the large one. Electromagnetic field simulators are commonly used to evaluate the inductance and coupling coefficient of metal pieces. On the other hand, they require substantial computation power and time.

To derive the inductances in the FMD system with low computation cost and short time, this work proposes a novel simulation method for foreign metal detection with magnetic field analysis. This work first estimates the magnetic field vector around the sense coil and metal piece using magnetics equations, then derives the virtual inductance of the metal piece and mutual inductance between the coil and the metal piece. The derived inductances allow us to build the equivalent circuit model that reproduces the impact of the metal piece, i.e., Z parameters.

The rest of this paper is organized as follows. Section II reviews the related work on FMD methods. Section III proposes a methodology that enables us to extract the equivalent circuit model of the metal piece in FMD system on the basis of magnetics. Section IV evaluates the proposed methodology in terms of its simulation accuracy and computation cost, and compares the performance with a general electromagnetic simulator. Section V discusses the limitation of the proposed methodology. Lastly, concluding remarks are given in Section VI.

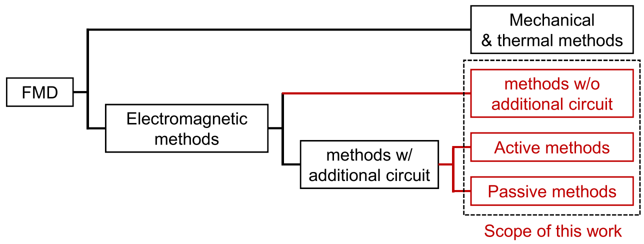

FIGURE 1. Classification of FMD methods by Xia et al. [31].

II. FOREIGN METAL DETECTION

FMD is one of the critical functions for IPT systems, as discussed in the previous section. This section reviews related research on FMD and highlights the contribution of this work. Xia et al. classified FMD methods into four categories based on the detection approach [31], as illustrated in Fig. 1. We introduce related work according to this classification.

FMD methods are first divided into those that utilize electromagnetic (EM) fields and those that do not. Non-EM field methods use sensors such as light, image, and temperature sensors [32], [33], [34], [35], [36]. Some of these methods can find not only foreign metal objects but also foreign living objects. However, these methods require relatively longer sensing time compared to EM field-based methods, which can react immediately after the insertion of foreign metal, since these methods monitor the effect of foreign metal indirectly. For this reason, FMD methods that utilize EM field are actively studied. This paper also focuses on EM field-based FMD. EM field-based methods are further divided into two methods that utilize an additional circuit or not. Additional circuit-based method is further classified into the active one and the passive one.

EM field-based methods without additional circuit utilize the power transmission circuit itself for FMD. The system detects foreign metals based on the circuit or other system parameter variations caused by the inserted foreign metal. One system parameter that can be measured easily is the power transmission efficiency or the transmission loss. Kuyvenhoven et al. propose the FMD method based on the power loss detection. Similarly, Kudo et al. report the FMD method that can detect foreign metal by monitoring the power transmission efficiency. Other methods detect foreign metal based on the variance of circuit parameter (e.g. impedance [37], current or voltage [31], [38], phase shift [39], frequency [40], [41], [42]). Refs. [31] and [43] explain these circuit parameter change and the transmission efficiency deterioration assuming the foreign metal as an inductor. If the foreign metal is placed in the vicinity of the IPT system, the transmission coil is weakly coupled with the metal piece pretending the inductor, and hence the mutual inductance between the power transmitter coil and the

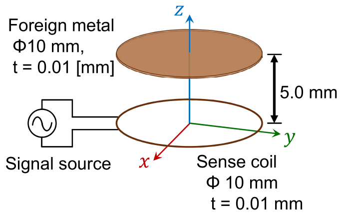

Execution profile

Name	Value
Real time *	29m 14s
CPU time *	77m 11s
Max. RAM usage	25.1 GB

* Processed in parallel with 12 threads.

FIGURE 2. Setup and execution profile of example simulation.

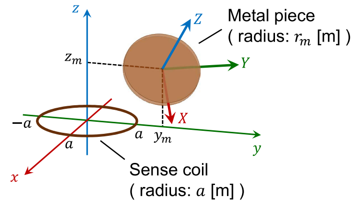

FIGURE 3. Problem formulation. A sense coil is placed in *xy*-plane and the center of the metal piece is on *yz*-plane.

receiver coil varies. This mutual inductance change causes the circuit and system parameter variance and can be utilized for FMD.

EM field-based methods requiring additional FMD circuits are based on the same methodology to regard the foreign metal as the inductor. Therefore, an additional circuit for FMD consists of an inductive circuit so that it can sense a subtle change in the mutual inductance. The difference between the active and passive circuit-based methods is the mutual inductance in which the system is interested. The active circuit-based methods focus on the mutual inductance between the sensing circuit and the foreign metal while the passive circuit-based methods focus on the mutual inductance between the sensing circuit and the power transmitter/receiver coil. As an active circuit-based method, S. Jeong et al. propose to sense the inductance variance of the sensing coil. The passive circuit-based FMD methods usually monitor the induced voltage at the sense coil [35], [43], [44], [45], where the induced voltage originates from the EM field for power transmission. When the foreign metal is placed nearby, the EM field is affected and the induced voltage is also changed. This voltage change is utilized for FMD.

As we explained above, many findings and methods related to FMD have been reported and accumulated. All EM-based FMD methods, which are mainstream FMD methods, focus on the inductance of the coil and foreign metal. Currently, all research is forced to utilize finite element method (FEM)-based EM field simulators, which require enormous computational resources and computational costs, for optimizing the FMD system configuration including the size and placement of the sensing coil. As an example, we conducted a simulation experiment of FMD with ANSYS HFSS, which is one of the widely used FEM-based EM simulators. Fig. 2 shows the simulation setup. Both the coil and the foreign metal have a circular shape and their diameter and thickness are 10 mm and 0.01 mm, respectively. We executed the simulation with a computer whose CPU is Intel i7-8700K and RAM is DDR4 16GB×4. Fig. 2 indicates that although we simulated with a parallel processing unit, the required real time is almost half an hour even for this simple and small structure. As for RAM, the maximum used RAM is more than 25 GB. This result demonstrate that the FEM-based EM simulator requires heavy computation even for the small and simple structures, making it impractical for design optimization. In addition, all research can evaluate its system only experimentally, and cannot evaluate analytically. This is because although we already know that the metal piece is approximated by an inductor, there is no methodology which allows us to extract its self and mutual inductance between the sensing coil and the metal piece analytically. Especially, the circuit model of a small metal piece, which is as severe as a large metal piece in terms of safety, is indispensable since the small metal piece is much harder to detect than the large metal.

For this reason, this work proposes a methodology for extracting the equivalent circuit of the small metal piece in FMD systems based on the theory of electromagnetics. The proposed methodology enables researchers and designers of FMD systems to treat the metal pieces as circuit elements with specific parameter values. This advantage frees designers and researchers from time-consuming FEM-based simulations, leading to reduced design costs and potentially enhanced safety. This is because our method reveals the unknown circuit parameters such as self and mutual inductances of the sense coil and the foreign metal, which allows researchers and designers to explore the system design analytically rather than experimentally.

III. PROPOSED METHODOLOGY

This section proposes an analytical simulation methodology for a foreign metal piece using the relationship between the sense coil and the metal piece on the basis of electromagnetic theory. First, Section III-A formulates our problem to be solved, and then Section III-B outlines the procedure our methodology. Successive Sections III-C, III-D, and III-E explain how to evaluate the inductance parameters in the FMD system by considering the magnetic flux density.

A. PROBLEM FORMULATION

As we explained in Section II, the mainstream of the FMD methods is EM-based ones, and all of the EM-based methods utilize the coil to detect the foreign metal object. Therefore, we assume Fig. 3 depicts the most simple form of the problem, in which only one sense coil and one foreign metal piece are included in the system. The sense coil is placed on the *xy*-plane, and the inclined metal piece locates in the vicinity of the sense coil. To simplify the mathematical discussions in the successive sections, we assume that both the sense coil and metal piece have circular shapes that are axially symmetrical, where a[m] and r_m[m] denote the diameters of the coil and the metal piece, respectively. We assume that the coil consists of the wire made of perfect

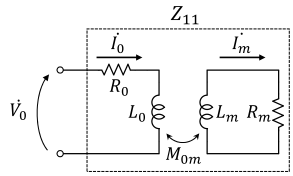

FIGURE 4. Equivalent circuit of the situation drawn in Fig. 3.

conductor whose diameter is w_0[m]. The thickness of the metal piece is ignored.

Fig. 4 shows an equivalent circuit expression of this situation. The system has only one port, and therefore the system behavior can be expressed by Z_{11} parameter since this system contains only the single sense coil and the coil is the single port element. R_0 and R_m in Fig. 4 denote the resistances of the sense coil and the foreign metal, respectively, and L_0 and L_m denotes the inductances of the sense coil and the foreign metal, respectively. M_{0m} is the mutual inductance between the sense coil and the metal piece.

As we can see from Fig. 3, we have to introduce several variables to explain the posture and position of the metal piece. Fig. 5 shows the definition of the coordinate system and variables to be utilized to represent the posture and position of the metal piece. Fig. 5 (a) shows two important coordinate systems: xyz-coordinate system, which is the absolute coordinate system, and XYZ-coordinate system, which is the metal piece coordinate system. As both the coil and metal piece are axially symmetrical, which is found in Fig. 3, the relative posture and position of the metal piece to the sensor coil have 4-Degrees of Freedom (DoF) and then are expressed by four variables: ϕ_z, ϕ_y, y_m and z_m. Originally in Fig. 3, the two coordinate systems are overlapping completely. First, we rotate the XYZ-coordinate system with the metal piece around Z-axis by ϕ_z[deg] ($0 \leq \phi_z \leq 90$) as shown in Fig.5(b). Then, we rotate the XYZ-coordinate system with the metal piece around Y-axis by ϕ_y[deg] ($-90 \leq \phi_y \leq 90$) as shown in Fig. 5(c). Finally we move the XYZ-coordinate system with the metal piece to the position of the coordinate of $(0, y_m, z_m)$[m], which is depicted in Fig. 5(d). By proceeding with these three steps, all relative posture and position are expressed.

To keep the discussion as simple as possible, we assume that the sense coil and the metal piece are made of perfect conductors and, hence the R_0 and R_m are zero. To validate this assumption, we conducted simulation experiments under the condition of $a = r_m = 2.5$[mm], $w_0 = 0.1$[mm], $\phi_y = \phi_z = 0$[deg], $y_m = 0$[m], and z_m is changed from 0.5 mm to 10 mm. This setup means the metal piece is on the z-axis and placed parallel to the sense coil. Fig 6 shows two HFSS simulation results: one is the result of the Z_{11} simulation with the copper foreign metal and another one is with the foreign metal made of perfect conductor. Fig. 6 indicates that the real part of the copper foreign metal is several mΩ at most and it decreases quickly according to an increase in z_m while the imaginary part is more than 600 mΩ at least. Therefore, the real part is less than 1 % of the imaginary part and the most dominant element determining Z_{11} value is the imaginary part of the Z_{11}. Fig. 6 also indicates that the imaginary part of Z_{11} is almost identical between the copper foreign metal and the perfect conductor. For these reasons, we can assume $R_0 = R_m = 0$. Besides, when the foreign metal is made of ferrous metallic material, the magnetic condition in the system becomes too complex for analytical discussion. Fortunately, on the other hand, the distortion of the electromagnetic field caused by the ferrous metallic material is larger compared to the non-ferrous one, which means the ferrous metallic material is much easier to be detected by the FMD system. Hence, this work assumes the foreign object is made of non-ferrous metallic material, which is much harder to be detected.

B. OVERVIEW OF THE PROPOSED METHODOLOGY

This section first introduces basic equations by analyzing the circuit shown in Fig. 4, and then explains variables required for deriving Z_{11} parameter.

KVL equations of the left and right side of the circuit in Fig. 4 are Eqs. (1) and (2), respectively.

$$\begin{cases} \dot{V}_0 = j\omega L_0 \dot{I}_0 + j\omega M_{0m} \dot{I}_m, & (1) \\ 0 = j\omega L_m \dot{I}_m + j\omega M_{0m} \dot{I}_0. & (2) \end{cases}$$

From Eq. (2), Eq. (3) is derived.

$$\dot{I}_m = -\frac{M_{0m}}{L_m} \dot{I}_0. \tag{3}$$

By substituting Eq.(3) into Eq. (1), Eq. (4) is obtained, where $\dot{V}_0$ is expressed only by $\dot{I}_0$.

$$\dot{V}_0 = j\omega L_0 \left(1 - k^2\right) \dot{I}_0, \tag{4}$$

where k is coupling coefficient between the sense coil and the foreign metal piece, and it is defined by Eq. (5).

$$k \stackrel{\text{def}}{=} \frac{M_{0m}}{\sqrt{L_0 L_m}}. \tag{5}$$

From Eq. (4), Z_{11} is obtained as Eq. (6).

$$Z_{11} = \frac{\dot{V}_0}{\dot{I}_0} = j\omega L_0 \left(1 - k^2\right). \tag{6}$$

Eq. (6) indicates that the variables required for deriving Z_{11} are only L_0 and k. k is derived from three components as shown in Eq. (5); namely the self inductance of the sense coil L_0, the self inductance of the metal piece L_m, and the mutual inductance between the coil and the metal piece M_{0m}. Each of the successive sections will derive values of these variables one by one analytically on the basis of the magnetic flux density.

C. SELF INDUCTANCE OF SENSING COIL

This section derives the self inductance of the sense coil L_0 whose winding number is one. Although the approximation method for deriving the self inductance of the single loop coil is reported decades ago [46], this section introduces the

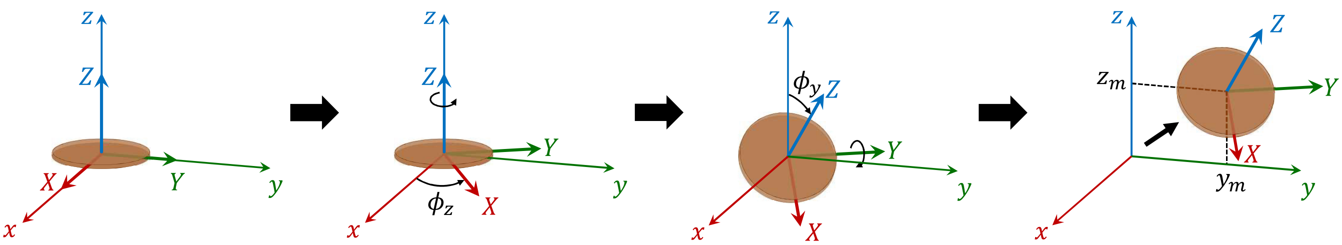

FIGURE 5. Posture and position of the metal piece. By rotating and moving the XYZ coordinate system according to (b), (c), and (d), all of the relative positions and postures of the metal piece with respect to the sense coil can be expressed. (a) xyz-coordinate system is the absolute coordinate system and XYZ-coordinate system is the metal piece coordinate system which determines the posture of the metal piece. Originally, these two coordinate systems are completely overlapping. (b) First, rotate XYZ-coordinate system and the metal piece around Z-axis by ϕ_z[deg] ($0 \le \phi_z \le 90$). (c) Then, rotate XYZ-coordinate system and the metal piece around Y-axis by ϕ_y[deg] ($-90 \le \phi_y \le 90$). (d) Finally, move XYZ-coordinate system and the metal piece on yz-plane so that the center of the metal piece goes to $(0, y_m, z_m)$ with respect to the xyz-coordinate system.

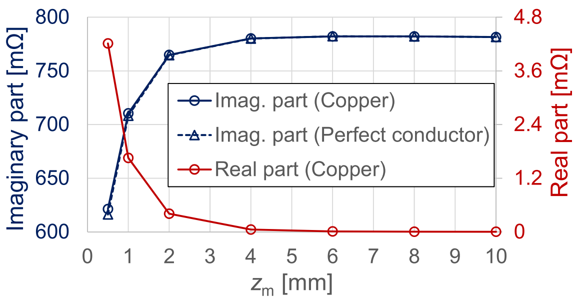

FIGURE 6. Variation of real and imaginary part of Z_{11} parameter when the signal frequency is 10 MHz, $w_0 = 0.1$[mm], $r_m = 2.5$[mm], $a = 2.5$[mm], $\phi_z = \phi_y = 0$[deg], $y_m = 0$[mm], and z_m is changed from 0.5 mm to 10 mm.

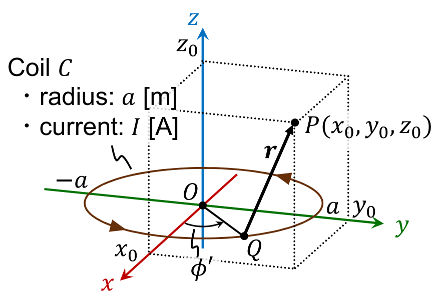

FIGURE 7. Coordinate setting and definition of variables.

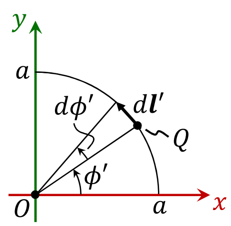

FIGURE 8. Definition of $d\phi'$ and dl'.

calculation method based on the magnetic flux density since the same basic idea will be applied to other inductance values in the successive sections.

The self inductance of a coil depends on the amount of the magnetic flux density generated by the coil itself. Hence, our primary objective is to derive an equation which can tell the magnetic flux density generated by the coil. Figs. 7 and 8 show the coordinate setting and definitions of the variables x_0, y_0, z_0, a, I, ϕ', $d\phi'$, and dl'. The sense coil is placed on the xy-plane, and the center of the coil is set to the origin of the xyz-coordinate system. When we inject the current I[A] to the sense coil C whose radius is a[m], the magnetic flux density $\boldsymbol{B}_P$ at the point P is obtained by calculating Eq. (7), which is based on Biot-Savart law [47].

$$\boldsymbol{B}_P = \oint_C d\boldsymbol{B} = \frac{\mu_0 I}{4\pi} \oint_C \frac{d\boldsymbol{l} \times \boldsymbol{r}}{|\boldsymbol{r}|^3}, \tag{7}$$

where μ_0 is the magnetic constant. Vectors $d\boldsymbol{l}$ and $\boldsymbol{r}$, and the magnitude $|\boldsymbol{r}|$ of the vector $\boldsymbol{r}$, appeared in Eq. (7) are given by Eqs. (8), (9), and (10), respectively.

$$d\boldsymbol{l} = a d\phi' \begin{bmatrix} -\sin\phi' \\ \cos\phi' \\ 0 \end{bmatrix}. \tag{8}$$

$$\begin{aligned} \boldsymbol{r} = \overrightarrow{QP} = \overrightarrow{OP} - \overrightarrow{OQ} &= \begin{bmatrix} x_0 \\ y_0 \\ z_0 \end{bmatrix} - \begin{bmatrix} a\cos\phi' \\ a\sin\phi' \\ 0 \end{bmatrix} \\ &= \begin{bmatrix} x_0 - a\cos\phi' \\ y_0 - a\sin\phi' \\ z_0 \end{bmatrix}. \end{aligned} \tag{9}$$

$$|\boldsymbol{r}| = \left\{x_0^2 + y_0^2 + z_0^2 + a^2 - 2a\left(x_0\cos\phi' + y_0\sin\phi'\right)\right\}^{1/2}. \tag{10}$$

By substituting Eqs. (8) and (9) into Eq. (7), we derive B_{Px}, B_{Py}, and B_{Pz}, which are x, y, and z components of the magnetic flux density $\boldsymbol{B}_P$, respectively, in Eq. (11):

$$\begin{aligned} \boldsymbol{B}_{Px} &= \frac{\mu_0 I a}{4\pi} \int_0^{2\pi} \frac{z_0 \cos\phi'}{|\boldsymbol{r}|^3} d\phi', \\ \boldsymbol{B}_{Py} &= \frac{\mu_0 I a}{4\pi} \int_0^{2\pi} \frac{z_0 \sin\phi'}{|\boldsymbol{r}|^3} d\phi', \\ \boldsymbol{B}_{Pz} &= \frac{\mu_0 I a}{4\pi} \int_0^{2\pi} \frac{a - x_0\cos\phi' - y_0\sin\phi'}{|\boldsymbol{r}|^3} d\phi'. \end{aligned} \tag{11}$$

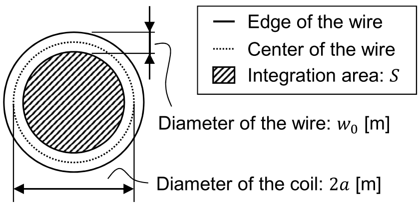

FIGURE 9. Integration area for deriving the self inductance of the sensing coil.

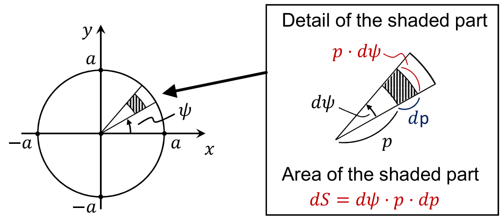

FIGURE 10. Area and position of minute part required for integration.

Here, $\boldsymbol{B}_P$ can be regarded as a vector function of a, I and $\boldsymbol{P}$, and B_{Px}, B_{Py}, and B_{Pz} satisfy the following relationship:

$$\boldsymbol{B}_P\left(a, I, \boldsymbol{P}\right) = \begin{bmatrix} B_{Px} \\ B_{Py} \\ B_{Pz} \end{bmatrix} = B_{Px} \cdot \boldsymbol{e}_x + B_{Py} \cdot \boldsymbol{e}_y + B_{Pz} \cdot \boldsymbol{e}_z, \tag{12}$$

where $\boldsymbol{P}$ denotes the position vector of the point P, and $\boldsymbol{e}_x$, $\boldsymbol{e}_y$, and $\boldsymbol{e}_z$ denote unit vectors pointing x, y, and z direction, respectively.

As we described at the beginning of this section, the self inductance of a coil depends on the magnetic flux density generated by the coil. In fact, the self inductance of the coil is defined as the amount of magnetic flux density that passes through the coil itself when a current of 1 A is applied to the coil. Therefore, the self inductance of the coil is obtained by integrating all the magnetic flux density perpendicular to the coil in the area surrounded by the wire. This is explained by Eq. (13).

$$L_0 = \int_S \boldsymbol{B}_P\left(a, 1, \boldsymbol{P}\right) \cdot \boldsymbol{e}_z \, dS = \int_S B_{Pz}\left(a, 1, \boldsymbol{P}\right) \, dS, \tag{13}$$

where $\boldsymbol{P}$ denotes all points in the integration area S. Eq. (13) calculates the inner product between $\boldsymbol{B}_P$ and $\boldsymbol{e}_z$ to extract the magnetic flux density which is perpendicular to the coil. In addition, the current injected to the coil is set to 1[A] by the definition of the self inductance. Fig. 9 shows the integration area, and it indicates that the integration area S is not identical to the circle whose radius is a. Instead, the integration area is the circular area whose radius is $a - w_0/2$[m]. Fig. 10 introduces two variables p and ψ to express dS. When the dp and $d\psi$ are infinitely small, dS is calculated by $dS = d\psi \cdot p \cdot dp$. By introducing these variables and the relationship, Eq. (13) becomes Eq.(14).

$$L_0 = \int_0^{a-\frac{w_0}{2}} \int_0^{2\pi} \boldsymbol{B}_P\left(a, 1, \begin{bmatrix} p\cos\psi \\ p\sin\psi \\ 0 \end{bmatrix}\right) \cdot \boldsymbol{e}_z \, d\psi \cdot p \cdot dp. \tag{14}$$

Eq. (14) gives the self inductance of the sense coil L_0. Meanwhile, Eq. (14) cannot be solved analytically, and hence we derive the inductance value by numerical integration. To conduct numerical integration, we divide the integration range of p and ψ into a finite number of parts. If we divide the integration range of p and ψ into n_p parts and n_ψ parts respectively, dp and $d\psi$ are described as Eq. (15).

$$dp = \frac{a - w_0/2}{n_p}, \quad d\psi = \frac{2\pi}{n_\psi}. \tag{15}$$

When dp and $d\psi$ are small enough, in other words, n_p and n_ψ are sufficiently large, Eq. (14) is approximated by Eq. (16).

$$L_0 = \sum_{i=1}^{n_p} \sum_{j=1}^{n_\psi} \boldsymbol{B}_P\left(a, 1, i\,dp \begin{bmatrix} \cos jd\psi \\ \sin jd\psi \\ 0 \end{bmatrix}\right) \cdot \boldsymbol{e}_z \, d\psi \cdot i \cdot dp^2, \tag{16}$$

where $p = idp$ and $\psi = jd\psi$ are applied.

D. MUTUAL INDUCTANCE BETWEEN SENSING COIL AND METAL PIECE

The mutual inductance between the sense coil and the metal piece is the amount of the magnetic flux density penetrating the metal perpendicularly. Therefore, the basic integration procedure is almost the same as the procedure for the self inductance of the coil in the previous subsection. The mutual inductance M_{0m} between the sense coil and the metal piece is expressed by Eq. (17).

$$M_{0m} = \int_{S'} \boldsymbol{B}_P\left(a, 1, \boldsymbol{P}_m\right) \cdot \boldsymbol{e}_Z \, dS', \tag{17}$$

where $\boldsymbol{P}_m$ is the point on the metal piece and $\boldsymbol{e}_Z$ is the unit vector pointing Z direction. The integration introduced in Eq. (17) is conducted on the metal piece, and therefore we have to know the coordinates of the point on the metal piece. As we described with Fig. 5, the posture and position of the metal piece are expressed by two rotations (ϕ_z and ϕ_y) and one shift ($+(0, y_m, z_m)$). These rotations and shift are considered to be a coordinate transformation from the xyz-coordinate system to the XYZ-coordinate system. Eq. (18) shows the rotational matrix for the rotation expressed by ϕ_z and ϕ_y.

$$\boldsymbol{R}\left(\phi_z, \phi_y\right) = \begin{bmatrix} \cos\phi_y\cos\phi_z & -\sin\phi_z & \sin\phi_y\cos\phi_z \\ \cos\phi_y\sin\phi_z & \cos\phi_z & \sin\phi_y\sin\phi_z \\ -\sin\phi_y & 0 & \cos\phi_y \end{bmatrix}. \tag{18}$$

Here, we assume that the metal piece has the circular shape, and hence the coordinates of the point $\boldsymbol{P}_{mo}$ on the metal piece are expressed by Eq. (19) as long as XYZ-coordinate system is completely overlapping with xyz-coordinate system.

$$\boldsymbol{P}_{mo} = \begin{bmatrix} p_m \cdot \cos\psi \\ p_m \cdot \sin\psi \\ 0 \end{bmatrix}. \tag{19}$$

By applying Eq. (18) to Eq. (19) and shifting the result by $+(0, y_m, z_m)$, the coordinates of the point $\boldsymbol{P}_m$ on the metal piece at any posture and place are given as Eq. (20).

$$\begin{aligned}\boldsymbol{P}_m &= \boldsymbol{R}\left(\phi_z, \phi_y\right)\boldsymbol{P}_{mo} + \begin{bmatrix} 0 \\ y_m \\ z_m \end{bmatrix} \\ &= \begin{bmatrix} p_m \cos\psi\cos\phi_y\cos\phi_z - p_m \sin\psi\sin\phi_z \\ y_0 + p_m\cos\psi\cos\phi_y\sin\phi_z + p_m\sin\psi\cos\phi_z \\ z_0 - p_m\cos\psi\sin\phi_y \end{bmatrix}.\end{aligned} \tag{20}$$

Evaluating Eq. (17) also requires the vector $\boldsymbol{e}_Z$. This vector $\boldsymbol{e}_Z$ is obtained by applying Eq. (18) to vector $\boldsymbol{e}_z$ as shown in Eq. (21).

$$\boldsymbol{e}_Z = \boldsymbol{R}\left(\phi_z, \phi_y\right)\boldsymbol{e}_z = \begin{bmatrix} \sin\phi_y\cos\phi_z \\ \sin\phi_y\sin\phi_z \\ \cos\phi_y \end{bmatrix}. \tag{21}$$

Finally, we need to set the integration area S' in Eq. (17). In Section III-C, we determined the integration area according to the radius of the coil and the diameter of the wire. In this section, we assume that a virtual loop coil can behave as a metal piece. The loop shape is discussed in the following.

As discussed with Eq. (6), we need the coupling coefficient k between the sense coil and the metal piece. The coupling coefficient k is defined by Eq. (5), and it depends on not only L_0 but also M_{0m} and L_m. Here, L_m is the virtual inductance of the metal piece and is determined by the current flow in the metal piece. The current flow in the metal piece is complex since the current can flow in any directions on the metal piece. Instead, for simplifying the discussion, we assume that the current flows only in a single specific loop whose thickness is zero. This assumption will be experimentally validated in Section IV-B. With this assumption, the current flow line is set to the edge of the metal piece or the boundary curve where the magnetic field vector along the Z direction becomes zero. The next paragraph exemplifies the assumed current flow.

Fig. 11 shows the integration area of two situations. The boundary between the integration area and the other consists of the locations at which the magnitude of the magnetic flux density pointing Z direction is zero. Therefore, the directions of the magnetic flux are different across the boundary in Fig. 11. In Fig. 11(a), the integration area is more than half of the metal piece area while the integration area in (b) occupies less area, where such difference originates from the relative location and posture of the metal piece from the sense coil. On the other hand, even in the situation like Fig. 11.(b), the sum of the magnitude of the magnetic flux density pointing Z direction is larger than those pointing $-Z$ direction. This is

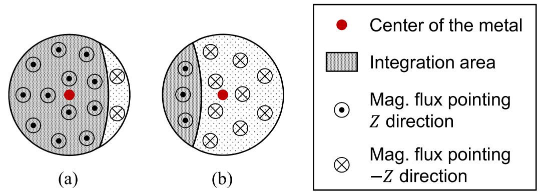

FIGURE 11. Relationship between the direction of the magnetic flux and integration area.

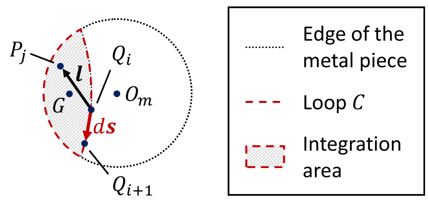

FIGURE 12. Definition of points, loop C, and the integration area on the metal piece.

because the magnitude of the magnetic flux density decays very quickly according to the distance from the sense coil as explained in Eq. (7). As a result, Eq. (17) is supposed to become Eq. (22) following the same procedure as Eq. (14).

$$M_{0m} = \int_0^{r_m - \frac{w_m}{2}} \int_0^{2\pi} f\left(\boldsymbol{B}_P\left(a, 1, \boldsymbol{P}_m\right) \cdot \boldsymbol{e}_Z\right) d\psi \cdot p_m \cdot dp_m, \tag{22}$$

where $f(x)$ is the clipping function introduced to eliminate the effect of the magnetic flux pointing $-Z$ direction and is defined as Eq. (23).

$$f(x) \stackrel{\text{def}}{=} \begin{cases} x & \text{if } x > 0, \\ 0 & \text{otherwise.} \end{cases} \tag{23}$$

w_m is the diameter of the virtual wire composing the virtual single loop coil that mimics the metal piece. We empirically determined the value of w_m as $w_m = 0.05\ r_m$, which denotes the width of the current flow is limited to the 5% of the metal piece radius. Similar to Eq. (16), Eq. (22) can also be transformed into the equation with sigma operator as shown in Eq. (24) so that we can evaluate M_{0m} numerically.

$$M_{0m} = \sum_{i=1}^{n_{pm}} \sum_{j=1}^{n_\psi} f\left(\boldsymbol{B}_P\left(a, 1, \boldsymbol{P}_m\right) \cdot \boldsymbol{e}_Z\right) d\psi \cdot i \cdot dp_m^2, \tag{24}$$

where n_{pm} and n_ψ denote the parameters that determine the discretization of the integration areas, and the others are defined as Eq. (25).

$$\begin{cases} dp_m = \dfrac{r_m - w_m/2}{n_{pm}}, \\ d\psi = \dfrac{2\pi}{n_\psi}, \\ p_m = i \cdot dp_m, \\ \psi = j \cdot d\psi. \end{cases} \tag{25}$$

E. SELF INDUCTANCE OF METAL PIECE

Finally, this section derives the inductance of the metal piece. As we described in the previous section, we treat the metal piece as the virtual single loop coil. We calculate the magnetic flux density generated by the virtual coil using the original Biot-Savart law instead of Eq. (7) since the virtual coil is not necessarily in a circular shape. We explain the procedure to derive the self inductance of the virtual loop coil supposing the situation in Fig. 11(b). Note that the situation in Fig. 11(a) can be discussed in the same way.

Fig. 12 shows the definition of points, vectors, the integration area, and loop C, which corresponds to the virtual loop coil discussed in the previous subsection. Point $Q_i(1 \leq i \leq n_C + 1)$ is one of the n_C points that divide loop C. Here, we assume that point Q_i and Q_{i+1} are located next to each other on loop C. We also assume Q_{n_C+1} denotes the same point as Q_1. Point G is the center of gravity of loop C, and it does not necessarily match with the center of the metal O_m. Point $P_j(1 \leq j \leq n_P)$ locates in the inside of loop C. We assume the integration area in Fig. 12 is divided into small n_P parts, and the center point and the area of each part are represented by point P_j and area dS_j, respectively. In this assumption, the magnetic flux density at point P_j is derived by Eq. (26) based on Biot-Savart law.

$$\boldsymbol{B}_{P_j} = \frac{\mu_0}{4\pi} \oint_C \frac{\boldsymbol{ds} \times \boldsymbol{l}}{|\boldsymbol{l}|^3}. \tag{26}$$

We derive inductance L_m of loop C by integrating Eq. (26) over the integration area in Fig. 12, S_m, as explained in Eq. (27).

$$L_m = \frac{\mu_0}{4\pi} \int_{S_m} \oint_C \frac{\boldsymbol{ds} \times \boldsymbol{l}}{|\boldsymbol{l}|^3} dS. \tag{27}$$

By introducing summation operator to Eq. (27), we obtain Eq. (28), which is suitable for numerical integration.

$$\begin{aligned} L_m &= \sum_{j=1}^{n_P} dS_j \cdot \frac{\mu_0}{4\pi} \sum_{i=1}^{n_C} \frac{\boldsymbol{ds}_i \times \boldsymbol{l}}{|\boldsymbol{l}|^3} \cdot \boldsymbol{e}_Z \cdot \prod_{h=1}^{n_C} g\left(\frac{|P_jQ_h|}{|GQ_h|}\right) \\ &= \frac{\mu_0}{4\pi} \sum_{j=1}^{n_P} dS_j \cdot \sum_{i=1}^{n_C} \frac{\overrightarrow{Q_iQ_{i+1}} \times \overrightarrow{Q_iP_j}}{|Q_iP_j|^3} \cdot \boldsymbol{e}_Z \\ &\quad \cdot \prod_{h=1}^{n_C} g\left(\frac{|P_jQ_h|}{|GQ_h|}\right). \end{aligned} \tag{28}$$

Here, the term of $\prod g$ works to limit the integration area so that the point which is too close to the loop C is not included in the integration result. Function $g(x)$, which is defined by Eq. (29), denotes that the point whose distance to loop C is less than 5% of the distance from loop C to the center of gravity G is ignored.

$$g(x) \stackrel{\text{def}}{=} \begin{cases} 1 & \text{if } x > 0.05, \\ 0 & \text{otherwise.} \end{cases} \tag{29}$$

Now, we have obtained the analytical equations that can calculate the self inductance of the coil (Eq. (16)), the mutual inductance between the coil and the metal piece (Eq. (24)), and the self inductance of the metal piece (Eq. (28)), which are required for describing the effect of the foreign metal piece. The next section will evaluate the performance of the methodology explained in this section and will introduce the comparison to a general FEM-based simulator in terms of the simulation accuracy and the computational cost.

IV. EVALUATION

This section shows simulation results based on our methodology and compares them with those of the FEM-based EM simulator. Section IV-A introduces the simulation result of the self inductance of the sense coil, and Section IV-B evaluates the Z_{11} parameter of the entire system by changing parameters y_m, z_m, ϕ_y and ϕ_z. Then, Section IV-C evaluates the frequency response of the system, and finally Section IV-D compares the computational cost between the simulator based on our methodology and ANSYS HFSS 16.1, which is a general FEM-based simulator. Here, all HFSS simulations in this section are executed at the signal frequency of 10 MHz.

A. SELF INDUCTANCE OF SENSE COIL

As we explained in Section III-C, the proposed methodology calculates the self inductance of the sense coil with numerical computation. There are two variables that define the shape of the sense coil: the diameter of the sense coil and the diameter of the wire. The following will demonstrate that our methodology can consider both of these variables.

Fig. 13 shows the self inductance evaluated by the simulator based on our methodology and ANSYS HFSS 16.1, where the coil diameter is 10 mm, and the wire diameter is changed from 30 μm to 500 μm. Fig. 13 indicates that the self inductance values are almost identical between this work and HFSS, and the error is below 2.85 %.

We also evaluate the self inductance of the sense coil whose wire diameter is 100 μm changing the coil diameter from 1mm to 50 mm assuming a FMD system that detects a small small metallic coin. Fig. 14 shows the simulation result. We can see that the inductance values are also highly correlated between this work and HFSS. The maximum error is 4.78 %, and the average error is 1.60 %.

These results indicate that our methodology can accurately estimate the self inductance of the sense coil. Here, note that the simulation error of a few percent is mostly negligible in practical use since the inductance of the commercially available inductors contains the error of several percentages. Also, the simulation result of the FEM-based method may include the error of several percentages depending on the mesh construction condition.

B. Z_{11} PARAMETERS AT SPECIFIC FREQUENCY

Next, we evaluate Z_{11} parameters in various situations since Z_{11} parameter can describe the effect of the metal piece as explained with Fig. 4. First, we show the relationship between the metal position and Z_{11} parameter. Then, we show how the rotation angle of the metal piece affects Z_{11} parameter.

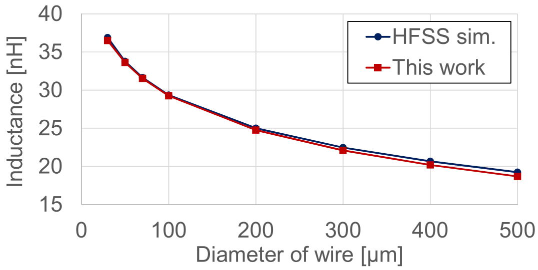

FIGURE 13. Comparison of the self inductance of the sense coil whose diameter is 10 mm and the diameter of the wire is changed from 30 μm to 500 μm.

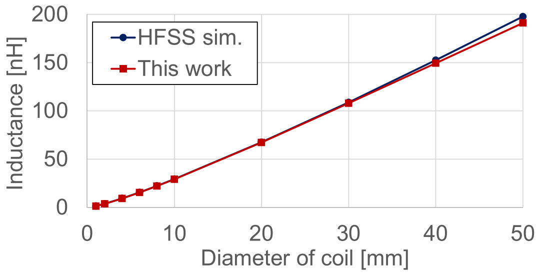

FIGURE 14. Comparison of the self inductance of the sense coil whose wire diameter is 100 μm and the diameter of the coil is changed from 1mm to 50 mm.

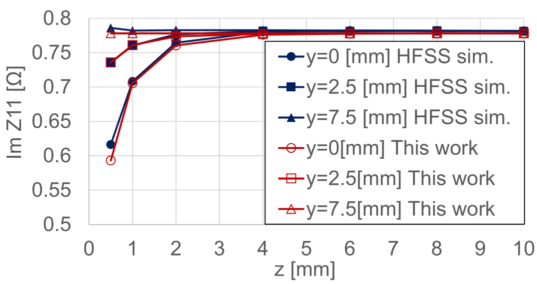

FIGURE 15. Comparison of Z_{11} parameter. z_m is changed from 0.5 mm to 10 mm, and y_m is changed from 0 mm to 7.5 mm. Diameters of the coil and the metal are both 5.0 mm. Rotation variables are set as $\phi_y = \phi_z = 0$[deg], and the wire diameter is 100 μm.

We conduct the following two simulation experiments to evaluate the relationship between the metal position and Z_{11} parameter. One experiment examines the situation that the radius of the metal piece is the same as the coil radius. The other experiment covers the situation that the radius of the metal piece is larger than the coil radius. Both experiments change z_m from 0.5 mm to 10 mm and y_m from 0 mm to 7.5 mm. Figs. 15 and 16 show the evaluation results indicating that our methodology can evaluate Z_{11} value accurately. The observed maximum error is 3.74 % and 3.11%, and the average error is 0.622 % and 0.663 %, respectively.

To evaluate the effect of the rotation angle of the metal piece on Z_{11} parameter comprehensively, we conduct four experiments, where Table 1 lists the variable combinations. Figs. 17 to 20 show the results. All the evaluations utilize the same sense coil and the metal piece, whereas y_m and ϕ_z are changed. In the setup of Fig. 17 ($y_m = 0$), the relative position is unchanged regarding ϕ_z since the center of the metal piece is on the z-axis and the sense coil has the axially symmetrical shape (See Fig. 5). Also, because of this symmetrical shape, the sweep of ϕ_y is limited to 0 degrees to 90 degrees. On the other hand, when non-zero value is set to y_m, the system structure is no longer symmetrical to z-axis. Therefore, for the case of ($y_m = 1$), we conduct three simulation experiments (Figs. 18 to 20), where the sweep range of ϕ_y is expanded to -90 degree to 90 degree. Here, in Figs. 18 to 20, the coil and the metal piece are physically intersected at several points, and therefore these points are not plotted. All of Figs. 18 to 20 indicate that the difference between the results based on our methodology and the HFSS results is small, and the tendency regarding the spatial location and rotation is completely reproduced by the proposed methodology. The average error in Figs. 17 to 20 is 0.365 %, and even the maximum error is only 1.55 %.

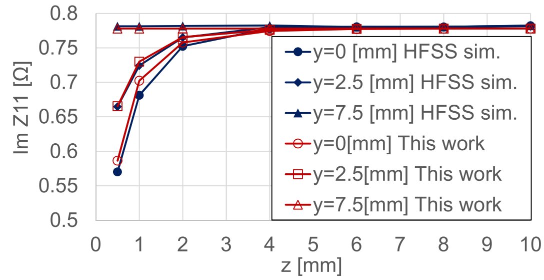

FIGURE 16. Comparison of Z_{11} parameter. z_m is changed from 0.5 mm to 10 mm, and y_m is changed from 0 mm to 7.5 mm. The diameter of the coil and the metal piece is 5.0 mm and 7.5 mm, respectively. Rotation variables are set $\phi_y = \phi_z = 0$[deg], and the wire diameter is 100 μm.

TABLE 1. Variable setup for Figs. 17 to 20.

Variable	Fig. 17	Fig. 18	Fig. 19	Fig. 20
a, r_m[mm]	2.5	2.5	2.5	2.5
y_m[mm]	0	1	1	1
w_0[µm]	100	100	100	100
ϕ_z[deg]	0	0	45	90

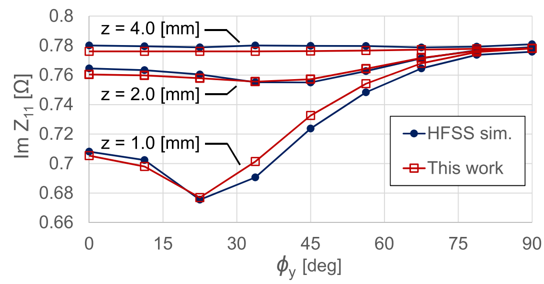

FIGURE 17. Relationship between ϕ_y and Z_{11}. Variables are set as $a = r_m = 2.5$[mm], $y_m = 0$[mm], $\phi_z = 0$[deg] and $w_0 = 100$[μm].

C. FREQUENCY RESPONSE

We next evaluate the reproducibility of the frequency response.

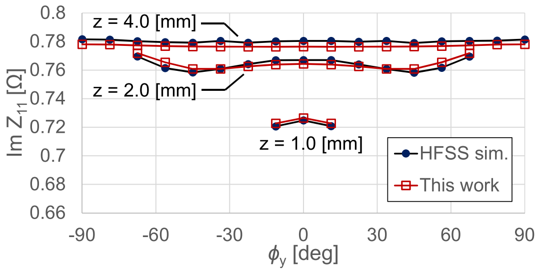

FIGURE 18. Relationship between ϕ_y and Z_{11}. Variables are set as $a = r_m = 2.5$[mm], $y_m = 1.0$[mm], $\phi_z = 0$[deg] and $w_0 = 100[\mu\text{m}]$.

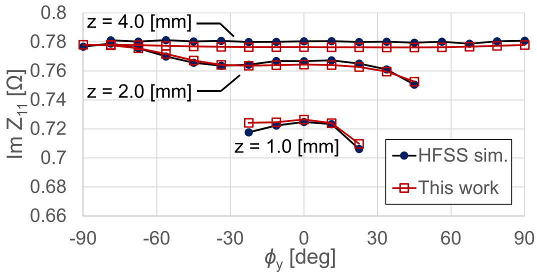

FIGURE 19. Relationship between ϕ_y and Z_{11}. Variables are set as $a = r_m = 2.5$[mm], $y_m = 1.0$[mm], $\phi_z = 45$[deg] and $w_0 = 100[\mu\text{m}]$.

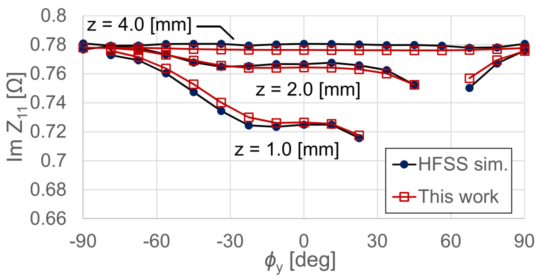

FIGURE 20. Relationship between ϕ_y and Z_{11}. Variables are set as $a = r_m = 2.5$[mm], $y_m = 1.0$[mm], $\phi_z = 90$[deg] and $w_0 = 100[\mu\text{m}]$.

We choose the following situation as an example: $a = r_m = 2.5$[mm], $y_m = 0$[mm], and $\phi_y = \phi_z = 0$[deg]. z_m is changed from 1 mm to 4mm. Fig. 21 shows the simulation result. The dotted line representing the proposed methodology completely overlaps with the solid line of the HFSS result. The average error is only 0.00405 % and the maximum error is 0.0131 %. This result indicates that our methodology is capable of evaluating the FMD system in the frequency domain.

D. COMPARISON OF COMPUTATIONAL COST

Lastly, we compare the computational cost between the simulator based on our methodology and HFSS. Our methodology does not utilize the mesh on which FEM-based EM simulators rely on, which contributes to fast computation with small memory usage. It should be noted that although the proposed methodology uses numerical integration with discretization, the number of divisions of numerical integration does not depend on the size and positional relationship between the coil and the metal piece. On the other hand, the number of mesh required for FEM, which affects the computation time and the RAM usage, highly depends on the the size and positional relationship between the coil and the metal piece.

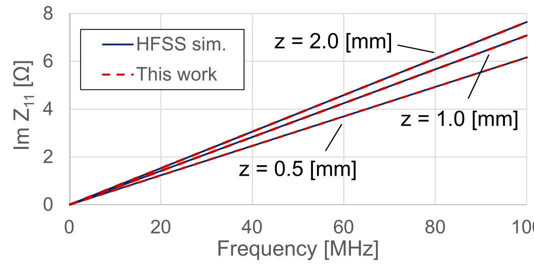

FIGURE 21. Comparison of the simulation result of the Z_{11} parameter in frequency domain. Variables are set as $a = r_m = 2.5$[mm], $y_m = 0$[mm], and $\phi_y = \phi_z = 0$[deg].

TABLE 2. Values of all parameters utilized in each case.

Variable	Case 1	Case 2	Case 3
a, r_m, z_m[mm]	2.5	5.0	10.0
y_m[mm]	0	0	0
w_0[µm]	30	30	30
ϕ_y, ϕ_z[deg]	0	0	0

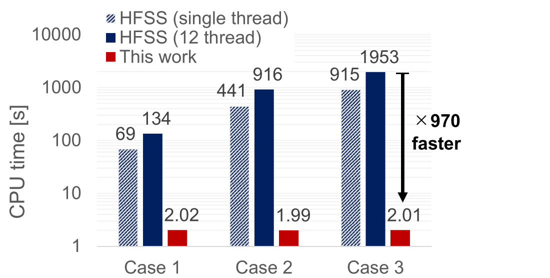

FIGURE 22. Comparison of CPU time between this work and HFSS. While this work computes the result with a single thread, HFSS evaluates the model both with single thread computing and 12 parallel threads computing.

To quantitatively compare the computational costs, we conducted simulation experiments with three setups listed in Table. 2. They cover various sizes of the system from several millimeter (case 1) to several centimeter (case 3). Here, in the HFSS simulation, we utilized a parallel thread computing unit to save the evaluation time while the simulator based on our methodology runs as a single thread. All evaluations were executed on a computer with a CPU of Intel i7-8700K and 64GB RAM. Figs. 22 and 23 show CPU time and memory usage, respectively. It should be noted that both Figs. 22 and 23 show the results in log scale. Fig. 22 shows that the CPU time of HFSS simulation increases according to the system size while the CPU times of our methodology are almost identical regardless of the system size. In case 3 of the largest system size, our approach gives the result 971 times faster compared with HFSS. The evaluation time of dozens of minutes with HFSS is shorted to several seconds with our methodology, which contributes to the acceleration of the FMD system design. Fig. 23 shows

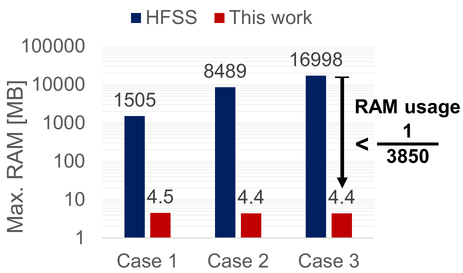

FIGURE 23. Comparison of RAM usage between this work and HFSS. While this work computes the result with a single thread, HFSS runs with 12 parallel threads.

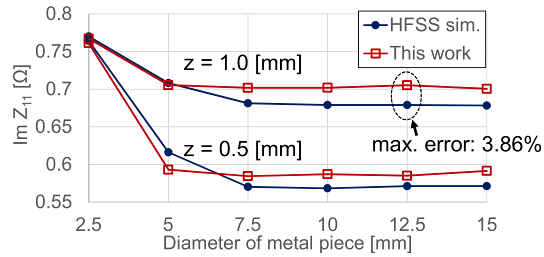

FIGURE 24. Variance of Z_{11} parameter when the relatively large metal piece is placed near the sense coil. Diameter of the sense coil is 5.0 mm, and $y_m = 0$[mm] $z_m = 0.5$[mm], $\phi_y = \phi_z = 0$[deg].

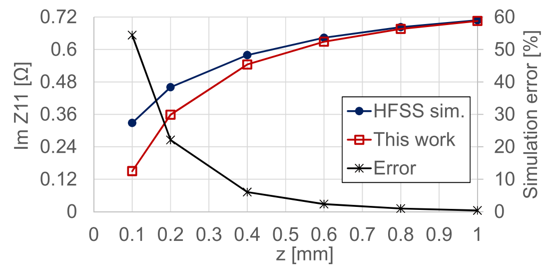

FIGURE 25. Variance of Z_{11} parameter when the metal piece is placed near the sense coil. Diameters of the sense coil and metal piece are both 5.0 mm, and $y_m = 0$[mm], $\phi_y = \phi_z = 0$[deg].

the RAM usage, indicating that the RAM usage of HFSS increases in GB order according to the system size, while our approach constantly consumes only 4.5 MB. In case 3, our approach reduced the memory usage to 1/3863. We confirm that our method always returns the result in almost the same CPU time with the same RAM usage. Thus, as the system size increases, the computational cost reduction becomes more significant.

V. LIMITATION

As we demonstrated in Section IV, the proposed methodology can evaluate the Z parameter in the FMD system quickly compared with the conventional FEM-based simulation method. On the other hand, our methodology has limitations that originate from two approximations. The first approximation is that we only consider the part of the metal piece where the magnetic flux density is pointing the Z-axis direction as we explained in Section III. The second approximation is an implicit one supposing that the current spread in Z-axis direction is infinitely small. These approximations may cause the evaluation error in two situations: (A) a relatively large metal piece is placed near the sense coil, and (B) a metal piece is placed in the vicinity of the coil. Let us discuss each situation.

A. LARGE METAL PIECE

When a relatively large metal piece is placed near the sense coil, our methodology cannot calculate both the equivalent self inductance of the metal piece and the mutual inductance between the sense coil and the metal piece correctly. This limitation comes from the limited integration area as we explained with Fig. 11 in Section III-D. Note that this issue arises only when the metal piece and the sense coil are much different in size, and it does not arise when both sizes are enlarged. Also, it should be mentioned that the relatively large metal piece is easily detected by the real FMD system, and hence the limitation discussed in this section does not disturb the system development.

To evaluate the effect of relative metal size on the calculation accuracy, we conduct a simulation supposing that the diameter of the sense coil is 5.0 mm, y_m is zero, and rotation angles ϕ_y and ϕ_z are both set to zero degrees. As for z_m, two setups of 0.5 and 1.0 [mm] are tested. Fig. 24 shows the comparison between this work and HFSS. The HFSS simulation results converge beyond 7.5 mm, while the results of our methodology are almost the same beyond 5.0 mm, where at the point of 5.0 mm, the diameters of the metal piece and the sense coil are the same. As for the converged values, our methodology overestimates Im Z_{11}, meaning that the coupling factor k calculated with our methodology is lower than the actual value. On the other hand, the error of Im Z_{11} is 3.88 % at most, as shown in Fig. 24. Besides, most of the system should tolerate such amount of error since even FEM-based methods may contain several percent error depending on the quality of the constructed mesh. Thus, we conclude that this error is not critical in terms of practicability.

B. VICINITY AREA OF COIL

As we mentioned at the beginning of this section, our methodology regards the thickness in Z-axis direction of the current flow line as zero. With this assumption, our methodology inherently suffers from the singular point issue, that is, the magnetic flux density becomes infinity as the measurement point approaches the current flow. To evaluate this effect, we conducted a simulation experiment with $a = r_m = 2.5$[mm], $\phi_y = \phi_z = 0$[deg], and $y_m = 0$[mm].

Fig. 25 shows the comparison between this work and HFSS. Im Z_{11} of our methodology becomes smaller than the HFSS result as the distance between the coil and the metal becomes smaller. This phenomenon originates from our assumption described above. When the metal piece locates near the coil wire, the magnetic flux density that penetrates the coil is calculated as almost infinity. Consequently, the coupling factor between the coil and the metal piece is overestimated. This overestimated coupling factor results in a lower Z_{11} value. The error caused by this phenomenon can be more than 50 % when the metal piece is placed 0.1 mm away from the coil.

We therefore limit the applicable region of the proposed methodology such that the metal piece should be placed apart from the coil at least the distance of one-tenth of the coil diameter. Meanwhile, this limitation is not a serious problem in terms of practical use since this prohibition region is sufficiently small compared to the size of the system. For example, when we use the sense coil whose diameter is 5.0 mm, the prohibition region is just 0.5 mm from the coil wire. Most of the research focuses on how to detect the metal piece apart from the sense coil since the metal piece placed near the sense coil can be easily detected. In addition, the situation in which the metal piece invades the prohibition region does not completely spoil the proposed method. Even in such a situation, the proposed method still can indicate the existence of the coil as shown in Fig. 25, and hence we suppose this limitation is acceptable.

VI. CONCLUSION

This paper proposed a methodology that analytically extracts equivalent circuits from the FMD systems. We established the simulation methodology with the aid of numerical integration to evaluate Z parameter of the system consisting of a sense coil and a metal piece. Our methodology can greatly reduce the computation cost to evaluate the FMD system since our methodology does not rely on FEM-based computation. We evaluated the accuracy and practicability of the proposed methodology using ANSYS HFSS 16.1 as a reference. Evaluation results showed that our simulation methodology can estimate Z_{11} parameter of the FMD system with a maximum error of only 3.88 % compared with HFSS. Also, our methodology can greatly reduce computational cost. The CPU time is reduced to 1/971, and the RAM usage is reduced to 1/3863 compared to HFSS. While our methodology has a prohibitive region, the methodology is practicable since the prohibition is limited to the region whose distance to the coil is within 1/10 of the coil diameter. The metal piece placed in such a small distance from the sense coil can be easily detected with general FMD methods, and hence the limitation stated above does not disturb the system development.

REFERENCES

[1] N. Tesla, "Apparatus for transmitting electrical energy," U.S. Patent 1 119 732, Dec. 1, 1914.
[2] N. Oodachi, H. Kudo, K. Ogawa, H. Shoki, S. Obayashi, and T. Morooka, "Efficiency improvement of wireless power transfer via magnetic resonance using the third coil," in *Proc. ISAP*, vol. 52, 2010, pp. 1–4.
[3] P. S. Riehl, A. Satyamoorthy, H. Akram, Y.-C. Yen, J.-C. Yang, B. Juan, C.-M. Lee, F.-C. Lin, V. Muratov, W. Plumb, and P. F. Tustin, "Wireless power systems for mobile devices supporting inductive and resonant operating modes," *IEEE Trans. Microw. Theory Techn.*, vol. 63, no. 3, pp. 780–790, Mar. 2015.
[4] A. Daga, J. M. Miller, B. R. Long, R. Kacergis, P. Schrafel, and J. Wolgemuth, "Electric fuel pumps for wireless power transfer: Enabling rapid growth in the electric vehicle market," *IEEE Power Electron. Mag.*, vol. 4, no. 2, pp. 24–35, Jun. 2017.
[5] S. Y. Hui, "Planar wireless charging technology for portable electronic products and Qi," *Proc. IEEE*, vol. 101, no. 6, pp. 1290–1301, Jun. 2013.
[6] Z. Bi, T. Kan, C. C. Mi, Y. Zhang, Z. Zhao, and G. A. Keoleian, "A review of wireless power transfer for electric vehicles: Prospects to enhance sustainable mobility," *Appl. Energy*, vol. 179, pp. 413–425, Oct. 2016.
[7] F. Lu, H. Zhang, and C. Mi, "A review on the recent development of capacitive wireless power transfer technology," *Energies*, vol. 10, no. 11, p. 1752, Nov. 2017.
[8] A. M. Jawad, R. Nordin, S. K. Gharghan, H. M. Jawad, and M. Ismail, "Opportunities and challenges for near-field wireless power transfer: A review," *Energies*, vol. 10, no. 7, p. 1022, Jul. 2017.
[9] G. K. Ottman, H. F. Hofmann, A. C. Bhatt, and G. A. Lesieutre, "Adaptive piezoelectric energy harvesting circuit for wireless remote power supply," *IEEE Trans. Power Electron.*, vol. 17, no. 5, pp. 669–676, Sep. 2002.
[10] H. F. Leung and A. P. Hu, "Modeling the contact interface of ultrasonic power transfer system based on mechanical and electrical equivalence," *IEEE J. Emerg. Sel. Topics Power Electron.*, vol. 6, no. 2, pp. 800–811, Jun. 2018.
[11] V. F. Tseng, S. S. Bedair, and N. Lazarus, "Acoustic wireless power transfer with receiver array for enhanced performance," in *Proc. IEEE Wireless Power Transf. Conf. (WPTC)*, May 2017, pp. 1–4.
[12] M. G. L. Roes, J. L. Duarte, M. A. M. Hendrix, and E. A. Lomonova, "Acoustic energy transfer: A review," *IEEE Trans. Ind. Electron.*, vol. 60, no. 1, pp. 242–248, Jan. 2013.
[13] A. Denisov and E. Yeatman, "Ultrasonic vs. inductive power delivery for miniature biomedical implants," in *Proc. Int. Conf. Body Sensor Netw.*, Jun. 2010, pp. 84–89.
[14] V. F. Tseng, S. S. Bedair, and N. Lazarus, "Phased array focusing for acoustic wireless power transfer," *IEEE Trans. Ultrason., Ferroelectr., Freq. Control*, vol. 65, no. 1, pp. 39–49, Jan. 2018.
[15] X. Bao, W. Biederman, S. Sherrit, M. Badescu, Y. Bar-Cohen, C. Jones, J. Aldrich, and Z. Chang, "High-power piezoelectric acoustic-electric power feedthru for metal walls," in *Industrial and Commercial Applications of Smart Structures Technologies*, vol. 6930. Bellingham, WA, USA: SPIE, 2008, Art. no. 69300Z.
[16] S. D. Jarvis, J. Mukherjee, M. Perren, and S. J. Sweeney, "Development and characterisation of laser power converters for optical power transfer applications," *IET Optoelectron.*, vol. 8, no. 2, pp. 64–70, 2014.
[17] J. Fakidis, S. Videv, S. Kucera, H. Claussen, and H. Haas, "Indoor optical wireless power transfer to small cells at nighttime," *J. Lightw. Technol.*, vol. 34, no. 13, pp. 3236–3258, Jul. 1, 2016.
[18] V. Iyer, E. Bayati, R. Nandakumar, A. Majumdar, and S. Gollakota, "Charging a smartphone across a room using lasers," *Proc. ACM Interact., Mobile, Wearable Ubiquitous Technol.*, vol. 1, no. 4, pp. 1–21, Jan. 2018.
[19] N. Shinohara, "Beam control technologies with a high-efficiency phased array for microwave power transmission in Japan," *Proc. IEEE*, vol. 101, no. 6, pp. 1448–1463, Jun. 2013.
[20] K. Huang and X. Zhou, "Cutting the last wires for mobile communications by microwave power transfer," *IEEE Commun. Mag.*, vol. 53, no. 6, pp. 86–93, Jun. 2015.
[21] E. Y. Chow, C.-L. Yang, Y. Ouyang, A. L. Chlebowski, P. P. Irazoqui, and W. J. Chappell, "Wireless powering and the study of RF propagation through ocular tissue for development of implantable sensors," *IEEE Trans. Antennas Propag.*, vol. 59, no. 6, pp. 2379–2387, Jun. 2011.
[22] J. Dai and D. C. Ludois, "A survey of wireless power transfer and a critical comparison of inductive and capacitive coupling for small gap applications," *IEEE Trans. Power Electron.*, vol. 30, no. 11, pp. 6017–6029, Nov. 2015.
[23] G. A. Covic and J. T. Boys, "Inductive power transfer," *Proc. IEEE*, vol. 101, no. 6, pp. 1276–1289, Jun. 2013.
[24] A. Kurs, A. Karalis, R. Moffatt, J. D. Joannopoulos, P. Fisher, and M. Soljačić, "Wireless power transfer via strongly coupled magnetic resonances," *Science*, vol. 317, no. 5834, pp. 83–86, Jul. 2007.
[25] *IEEE standard for Safety Levels With Respect to Human Exposure to Electric, Magnetic, and Electromagnetic Fields, 0 Hz to 300 GHz*, IEEE Standard C95.1-2019 (Revision IEEE Standard C95.1-2005/ Incorporates IEEE Standard C95.1-2019/Cor 1-2019), 2019, pp. 1–312.
[26] A. S. Y. Poon, S. O'Driscoll, and T. H. Meng, "Optimal frequency for wireless power transmission into dispersive tissue," *IEEE Trans. Antennas Propag.*, vol. 58, no. 5, pp. 1739–1750, May 2010.
[27] M. Mark, T. Björninen, L. Ukkonen, L. Sydänheimo, and J. M. Rabaey, "SAR reduction and link optimization for mm-size remotely powered wireless implants using segmented loop antennas," in *Proc. IEEE Topical Conf. Biomed. Wireless Technol., Netw., Sens. Syst.*, Jan. 2011, pp. 7–10.

[28] Y.-T. Liao, H. Yao, A. Lingley, B. Parviz, and B. P. Otis, "A 3-μW CMOS glucose sensor for wireless contact-lens tear glucose monitoring," *IEEE J. Solid-State Circuits*, vol. 47, no. 1, pp. 335–344, Jan. 2012.

[29] N. Kuyvenhoven, C. Dean, J. Melton, J. Schwannecke, and A. E. Umenei, "Development of a foreign object detection and analysis method for wireless power systems," in *Proc. IEEE Symp. Product Compliance Eng.*, Oct. 2011, pp. 1–6.

[30] W. P. Consortium, "Qi System description wireless power transfer volume I: Low power Part 1: Interface definition version 1.1," Wireless Power Consortium, Piscataway, NJ, USA, Tech. Rep., 2012.

[31] J. Xia, X. Yuan, J. Li, S. Lu, X. Cui, S. Li, and L. M. Fernández-Ramírez, "Foreign object detection for electric vehicle wireless charging," *Electronics*, vol. 9, no. 5, p. 805, May 2020.

[32] J.-W. Jeong, S.-H. Ryu, B.-K. Lee, and H.-J. Kim, "Tech tree study on foreign object detection technology in wireless charging system for electric vehicles," in *Proc. IEEE Int. Telecommun. Energy Conf. (INTELEC)*, Oct. 2015, pp. 1–4.

[33] P. F. Hoffman, R. J. Boyer, and R. A. Henderson, "Foreign object detection system and method suitable for source resonator of wireless energy transfer system," U.S. Patent 9 304 042, Apr. 5, 2016.

[34] T. Sonnenberg, A. Stevens, A. Dayerizadeh, and S. Lukic, "Combined foreign object detection and live object protection in wireless power transfer systems via real-time thermal camera analysis," in *Proc. IEEE Appl. Power Electron. Conf. Expo. (APEC)*, Mar. 2019, pp. 1547–1552.

[35] S. Verghese, M. P. Kesler, K. L. Hall, and H. T. Lou, "Foreign object detection in wireless energy transfer systems," U.S. Patent 9 442 172, Sep. 13, 2016.

[36] H. Widmer, L. Sieber, A. Daetwyler, and M. Bittner, "Systems, methods, and apparatus for radar-based detection of objects in a predetermined space," U.S. Patent 9 772 401, Sep. 26, 2017.

[37] Y.-C. Wang and C.-W. Chiang, "Foreign metal detection by coil impedance for EV wireless charging system," in *Proc. EVS Int. Electr. Vehicle Symp. Exhib. (KINTEX)*, Goyang, South Korea, 2015, pp. 3–6.

[38] Z. N. Low, J. J. Casanova, P. H. Maier, J. A. Taylor, R. A. Chinga, and J. Lin, "Method of load/fault detection for loosely coupled planar wireless power transfer system with power delivery tracking," *IEEE Trans. Ind. Electron.*, vol. 57, no. 4, pp. 1478–1486, Apr. 2010.

[39] S.-J. Huang, J.-L. Su, S.-H. Dai, C.-C. Tai, and T.-S. Lee, "Enhancement of wireless power transmission with foreign-object detection considerations," in *Proc. IEEE 6th Global Conf. Consum. Electron. (GCCE)*, Oct. 2017, pp. 1–2.

[40] M. Moghaddami and A. I. Sarwat, "A sensorless conductive foreign object detection for inductive electric vehicle charging systems based on resonance frequency deviation," in *Proc. IEEE Ind. Appl. Soc. Annu. Meeting (IAS)*, Sep. 2018, pp. 1–6.

[41] H. Jafari, M. Moghaddami, and A. I. Sarwat, "Foreign object detection in inductive charging systems based on primary side measurements," *IEEE Trans. Ind. Appl.*, vol. 55, no. 6, pp. 6466–6475, Nov. 2019.

[42] B. Regensburger, A. Kumar, S. Sinha, K. Doubleday, S. Pervaiz, Z. Popovic, and K. Afridi, "High-performance large air-gap capacitive wireless power transfer system for electric vehicle charging," in *Proc. IEEE Transp. Electrific. Conf. Expo (ITEC)*, Jun. 2017, pp. 638–643.

[43] L. Xiang, Z. Zhu, J. Tian, and Y. Tian, "Foreign object detection in a wireless power transfer system using symmetrical coil sets," *IEEE Access*, vol. 7, pp. 44622–44631, 2019.

[44] C. Qi, T. Lin, Z. Wang, D. Li, and T. Sun, "Research on metal object detection of MCR-WPT system that allows transmisson coils to be misaligned," in *Proc. 45th Annu. Conf. IEEE Ind. Electron. Soc. (IECON)*, vol. 1, Oct. 2019, pp. 4642–4647.

[45] V. X. Thai, G. C. Jang, S. Y. Jeong, J. H. Park, Y.-S. Kim, and C. T. Rim, "Symmetric sensing coil design for the blind-zone free metal object detection of a stationary wireless electric vehicles charger," *IEEE Trans. Power Electron.*, vol. 35, no. 4, pp. 3466–3477, Apr. 2020.

[46] F. Ternan, *Radio Engineers Handbook*. New York, NY, USA: McGraw-Hill, 1943, p. 472.

[47] D. K. Cheng, *Fundamentals of Engineering Electromagnetics*. Boston, MA, USA: Addison-Wesley, 1993.

RYO SHIRAI (Member, IEEE) received the B.E., M.E., and Ph.D. degrees in information systems engineering from Osaka University, Suita, Japan, in 2016, 2018, and 2021, respectively. He is currently an Assistant Professor with the Department of Communication and Computer Engineering, Graduate School of Informatics, Kyoto University, Kyoto, Japan. His current research interests include analog circuit design, embedded systems, and sensor systems. He is a member of the Institute of Electronics, Information and Communication Engineers (IEICE).

GORO NAKAO received the B.E. and M.E. degrees in electrical and electronic engineering from Shinshyu University, Nagano, Japan, in 2002 and 2004, respectively. He is currently with OMRON Corporation, Aichi, Japan. His current research interests include analog circuit design and wireless power transfer.

MASANORI HASHIMOTO (Senior Member, IEEE) received the B.E., M.E., and Ph.D. degrees in communications and computer engineering from Kyoto University, Kyoto, Japan, in 1997, 1999, and 2001, respectively. He is currently a Professor with the Department of Communications and Computer Engineering, Kyoto University. His current research interests include the design for manufacturability and reliability, timing and power integrity analysis, reconfigurable computing, soft error characterization, and low-power circuit design. He was a recipient of the Best Paper Award from Asia and South Pacific Design Automation Conference, in 2004; and the Best Paper Award of the IEICE Transactions, in 2016. He served as the Program Chair for ASP-DAC and the Program Co-Chair for MWSCAS. He was on the Technical Program Committee of international conferences, including Design Automation Conference, International Conference on Computer Aided Design, International Test Conference, Symposium on VLSI Circuits, ASP-DAC, and DATE. He serves/served as the Editor-in-Chief for *Microelectronics Reliability* (Elsevier); and an Associate Editor for IEEE Transactions on Very Large Scale Integration Systems, IEEE Transactions on Circuits and Systems:—I, and *ACM Transactions on Design Automation of Electronic Systems*.